PNAS RESEARCH ARTICLE | BIOPHYSICS AND COMPUTATIONAL BIOLOGY

A geometric-tension-dynamics model of epithelial convergent extension

Nikolas H. Claussen[a,1], Fridtjof Brauns[b,1,2], and Boris I. Shraiman[a,b,2]

Affiliations are included on p. 10.

Edited by Bulbul Chakraborty, Brandeis University, Waltham, MA; received December 13, 2023; accepted August 17, 2024 by Editorial Board Member Mehran Kardar

Convergent extension of epithelial tissue is a key motif of animal morphogenesis. On a coarse scale, cell motion resembles laminar fluid flow; yet in contrast to a fluid, epithelial cells adhere to each other and maintain the tissue layer under actively generated internal tension. To resolve this apparent paradox, we formulate a model in which tissue flow in the tension-dominated regime occurs through adiabatic remodeling of force balance in the network of adherens junctions. We propose that the slow dynamics within the manifold of force-balanced configurations is driven by positive feedback on myosin-generated cytoskeletal tension. Shifting force balance within a tension network causes active cell rearrangements (T1 transitions) resulting in net tissue deformation oriented by initial tension anisotropy. Strikingly, we find that the total extent of tissue deformation depends on the initial cellular packing order. T1s degrade this order so that tissue flow is self-limiting. We explain these findings by showing that coordination of T1s depends on coherence in local tension configurations, quantified by a geometric order parameter in tension space. Our model reproduces the salient tissue- and cell-scale features of germ band elongation during *Drosophila* gastrulation, in particular the slowdown of tissue flow after approximately twofold elongation concomitant with a loss of order in tension configurations. This suggests local cell geometry contains morphogenetic information and yields experimentally testable predictions. Defining biologically controlled active tension dynamics on the manifold of force-balanced states may provide a general approach to the description of morphogenetic flow.

force balance | active T1s | cell packing | *Drosophila* embryo | active solid

Significance

Animal development requires large numbers of cells to choreograph their force generation in order to sculpt tissues and organs. Leveraging the fact that cellular forces equilibrate rapidly compared to the speed of development, we formulate a geometrical model for the network of balanced active tensions in an epithelial sheet. Within this framework, we can investigate how cells remodel the tension network to change tissue shape. A simple "winner-takes-all" mechanical feedback loop can self-organize complex cell movement, matching experimental data on the cell and tissue scale. We find that the ability to self-organize depends on initial order in the cellular packing. Our model explains how genetic patterning, embryo geometry, and cellular packing geometry combine to determine tissue shape change.

Shape changes of epithelia during animal development involve major cell rearrangements, often manifested as a "convergent extension" of cell sheets (CE). On the coarse scale, CE resembles the laminar shear flow of an incompressible fluid in the vicinity of a hyperbolic fixed point (Fig. 1*A*). Indeed, previous work has combined hydrodynamic equations for the mesoscale cell velocity field with active stress fields to model morphogenetic tissue flow (1–4). Yet in contrast to a fluid, epithelia are under internally generated tension—as revealed by laser ablation (5)—and, like solids, maintain their shape against external forces. Tissue flow is achieved through local cell intercalation (T1 neighbor exchange processes; see Fig. 1*B*) driven by the concerted mechanical activity of individual cells. Cells generate forces via actomyosin contractility in the cortical cytoskeleton at the adherens junctions between cells (Fig. 1*C*). Moreover, the adherens junctions can remodel through the turnover of their constituent molecules: Interfaces in the cell array can change their length and tension independently. This behavior is fundamentally different from (Hookean) springs, where tension and length are related by a constitutive relationship. Instead, one can imagine cellular interfaces as "microscopic muscles" which are actuated by the recruitment and release of myosin motors.

Vertex models generally describe epithelial tissue as a polygonal tiling of cells where the vertex positions are the dynamical variables (6, 7). The forces that drive the vertex motion are commonly derived from passive area and perimeter elasticity supplemented with additional active tensions (8–10). However, the muscle metaphor for cellular interfaces suggests that active tension is central to the mechanical network underlying an epithelial tissue (Fig. 1*D*). This network rapidly equilibrates to a force balanced state (5, 11, 12), stabilized by mechanical feedback loops (13, 14). In such an active tension network, passive (bulk) elasticity plays a subdominant role. The need for stabilizing feedback loops arises because active tensions are untethered from interface lengths. Indeed, on an abstract level, these feedback loops are not unlike the regulatory mechanisms that control and stabilize skeletal musculature (15).

Here, we propose that tissue flow can be understood in the terms of adiabatic (quasi-static) remodeling of internal active force balance. Force balance in the cortical

Author contributions: N.H.C., F.B., and B.I.S. designed research; N.H.C. and F.B. performed research; F.B. analyzed data; N.H.C. implemented numerical simulations; and N.H.C., F.B., and B.I.S. wrote the paper.

The authors declare no competing interest.

This article is a PNAS Direct Submission. B.C. is a guest editor invited by the Editorial Board.

Copyright © 2024 the Author(s). Published by PNAS. This article is distributed under Creative Commons Attribution-NonCommercial-NoDerivatives License 4.0 (CC BY-NC-ND).

[1]N.H.C. and F.B contributed equally to this work.

[2]To whom correspondence may be addressed. Email: fbrauns@kitp.ucsb.edu or shraiman@kitp.ucsb.edu.

This article contains supporting information online at https://www.pnas.org/lookup/suppl/doi:10.1073/pnas.2321928121/-/DCSupplemental.

Published September 27, 2024.

Downloaded from https://www.pnas.org by UC Santa Barbara on July 22, 2025 from IP address 169.231.119.112.

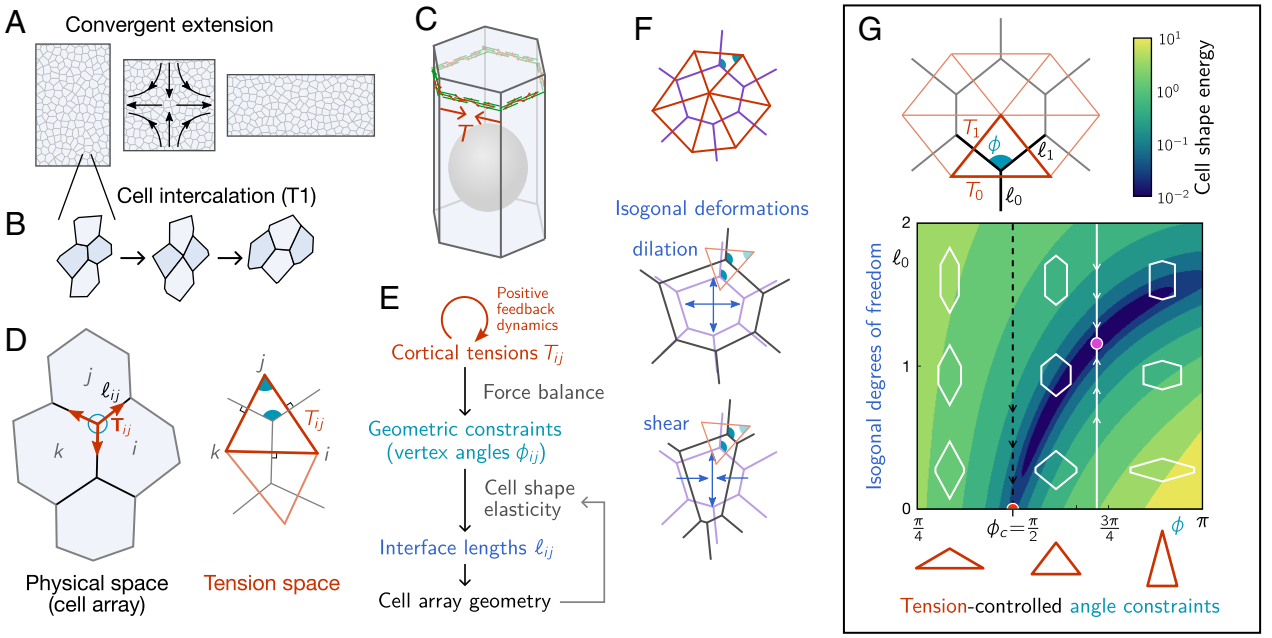

Fig. 1. A model for tissue mechanics dominated by cortical tension. (*A*) Convergent extension (CE) of epithelial tissue by cell intercalations (T1 processes, *B*). (*C*) A single cell from a columnar epithelium with the actomyosin cortex at the adherens junction belt generating tension T along cell–cell interfaces. Gray sphere represents the nucleus. (*D*) In force balance, the tensile forces $\mathbf{T}_{ij}$ at each vertex must sum to zero, implying that they form a triangle. The angles in the tension triangulation are complementary to the angles in the cell array, thus linking tension space to physical space. Force balance implies that the tensile force vectors at each vertex form a triangle. (*E*) Schematic outline of our quasi-static tissue model with mechanics dominated by actively regulated cortical tensions (see text for details). (*F*) Illustration of isogonal deformations of a reference geometry (purple) that is dual to the tension triangulation (red). (*G*) Implementation of the model for a symmetric, regular cell array, characterized by one angle ϕ, determined by the tensions T_0, T_1, and two lengths, ℓ_0 and ℓ_1, parameterizing the soft isogonal modes. The contour plot shows the cell shape energy $E_\mathcal{C}$ in the incompressible limit where ℓ_1 is determined uniquely by ℓ_0 and ϕ. Relaxation of the subdominant cell shape energy $E_\mathcal{C}$ is constrained to the isogonal subspace (white line) determined by tension force balance. For the critical tension ratio $T_0/T_1 = \sqrt{2}$ (corresponding to $\phi_c = \pi/2$, black dashed line), the interface length minimizing $E_\mathcal{C}$ vanishes (red half-disk). See Movie S1 for an animated version.

tension network defines a manifold of cellular tiling geometries on which tissue deformation unfolds. We propose that dynamics in the force-balance manifold is driven by positive feedback on the cortical tensions. This view is supported by analysis of high-quality live imaging data (16) from *Drosophila* gastrulation presented in the companion paper (17). Specifically, a geometric active–passive decomposition as well as mutant analysis were used to show that tissue flow is driven by internally generated tension dynamics, rather than external forces. Tension inference has provided evidence for the role of positive tension feedback during active T1 events. Numerical simulations of cell quartets show that such a feedback mechanism is sufficient to drive the T1 process. However, the key question of coordination of T1s across the tissue—required to drive coherent tissue flow—has remained unanswered. To address this question, we develop a model of tissue mechanics in the tension-dominated regime and demonstrate via numerical simulations how positive feedback drives CE. We show that order of the cell packing is necessary for coordinating T1 processes, and hence efficient CE. T1s destroy this order such that the extent of tissue flow is self-limiting. Thereby, our model reproduces the experimentally observed elongation of the germband where the arrest of flow is concomitant with a transition from an ordered to a disordered cell packing (17).

Methods

A Minimal Model Based on Force Balance and Cell Geometry. Our model is based on two assumptions: a) on morphogenetic timescales, the forces in the epithelium are approximately balanced, and b) active cortical tensions (generated by contractile actomyosin along the adherens junctions Fig. 1*C*) dominate over all other sources of stress. In particular, we assume that adhesion forces between the epithelial layer and its substrate (the fluid yolk and perivitelline fluid (18) for the *Drosophila* embryo) are negligible. Hence, all forces must be balanced within the transcellular network of cellular junctions. We model the tissue in the framework of vertex models (see e.g. ref. 7) as a polygonal tiling of the plane with tricellular vertices $\mathbf{r}_{ijk}$, where each polygon represents a cell i (Fig 1*D*). We write the elastic energy differential of this network as

$$dE(\{\mathbf{r}_{ijk}\}|\{T_{ij}\}) = \sum_{ij} T_{ij} d\ell_{ij} - p \sum_i dA_i + \varepsilon \sum_i dE_\mathcal{C}(S_i), \qquad [1]$$

where ε is a small parameter that separates the dominant scale of active tension and subdominant passive mechanical contributions from bulk and shear elasticity of the cell interior. $E_\mathcal{C}(S_i)$ accounts for the passive elasticity of the cells and will be specified below; $\ell_{ij} = ||\mathbf{r}_{ij}||$ and T_{ij} are the length of and tension along the interface between adjacent cells i and j. Importantly, in contrast to the standard vertex model where edge tension is defined by a constitutive relation corresponding to a passive Hookean perimeter spring, we take cortical tensions to be controlled independently of the interface lengths. The tension dynamics is described in the next section. The second term in Eq. **1** accounts for the effective in-plane pressure p of the cells that, by maintaining the total surface area (sum over cell areas A_i), ensures that the tissue as a whole does not collapse. In the *Drosophila* embryo, the closed epithelial sheet encloses the yolk, which is under pressure, balancing the cortical tensions. Other epithelia are kept under tension via traction forces at the boundary (19). We assume that pressure differences between cells are small and therefore absorb them into $E_\mathcal{C}(S_i)$. In experimental data, this can be verified by inspecting the curvature of cell–cell interfaces: Due to the Laplace law, significant pressure differences would manifest through curved cell–cell interfaces which are not observed in the early *Drosophila* embryo prior to the onset of cell divisions (12, 16, 17, 20).

As noted, we assume a separation of scales between the timescale on which the elastic energy relaxes and the timescale on which the tissue deforms

Downloaded from https://www.pnas.org by UC Santa Barbara on July 22, 2025 from IP address 169.231.119.112.

macroscopically. In terms of relaxational dynamics $\gamma \partial_t \mathbf{r}_{ijk} = -\frac{\partial E}{\partial \mathbf{r}_{ijk}}$, we consider a relaxation rate–set by the coefficient of friction γ–much faster than all other timescales in the system. Quasi-static force balance implies

$$\frac{\partial E}{\partial \mathbf{r}_{ijk}} = 0. \quad [2]$$

Solving this equation to zeroth order in ϵ yields a force-balance constraint at each vertex: The tension vectors $\mathbf{T}_{ij} = T_{ij}\mathbf{e}_{ij}$ at each vertex must sum to zero and hence form a triangle as illustrated in Fig. 1*D*. Since neighboring vertices share the interface that connects them, the corresponding tension triangles share an edge. Therefore, all tension triangles have to fit together: They form a triangulation that is dual to the cell tiling (13, 21, 22). This tension triangulation is a geometric manifestation of global force balance in the tissue, where angles at real-space vertices are complementary to the corresponding angles in the tension triangle (Fig. 1*D*).

Importantly, the angles at vertices *do not* fully determine the geometry of the cell tessellation, i.e. the vertex positions $\mathbf{r}_{ijk}$: one can change the interface lengths ℓ_{ij} while preserving all angles. The resulting isogonal soft modes* account for interface length changes under constant tension (13), which is possible thanks to the turnover of cytoskeletal elements.

The isogonal modes can dilate and shear cells (Fig. 1*F*). They are soft modes of the leading order elastic energy and thus force us to take into account subleading contributions to arrive at a complete model of tissue mechanics. Cells resist shape distortions due to rigid cell-internal structures such as microtubules, the nucleus (23, 24), and intermediate filaments (25). To account for this passive cell elasticity, we propose an energy

$$E_{\mathcal{C}}(S) = \lambda[\mathrm{Tr}(S - S_0)]^2 + \mu \mathrm{Tr}[(S - S_0)^2], \quad [3]$$

in terms of the cell shape tensor

$$S_i = \sum_{k \in \mathcal{N}_i} \frac{\mathbf{r}_{ik} \otimes \mathbf{r}_{ik}}{\ell_{ik}}, \quad [4]$$

where $\mathcal{N}_i$ is the set neighbors of cell i. This shape energy effectively models the cell interior as a homogeneous elastic material (26). (In *SI Appendix*, section 5, we compare this elastic energy with the often-used "area–perimeter" elastic energy which we find produces qualitatively different behavior incompatible with experimental observations.) The shape tensor is defined to be invariant under subdivision of interfaces. The reference tensor S_0 controls the target cell shape and is given by $S_0 = 3\ell_0 \mathbb{I}$ for an isotropic hexagonal cell with side length ℓ_0. We relate cell and tissue elasticity by analyzing the energy spectrum of isogonal modes for a fixed tension triangulation (*SI Appendix*, section 4). The isogonal modes with the lowest energy correspond to large-scale shears and thus provide a linear relationship between the cell and tissue shear moduli (*SI Appendix*, Fig. S13).†

For sufficiently small values of the scale-separation parameter ϵ, minimization of the elastic energy Eq. **1** can be performed in two separate steps: First, force balance of the dominant cortical tensions T_{ij} fixes the angles at vertices thus setting geometric constraints. Second, the subleading term $\sum_i E_{\mathcal{C}}(S_i)$ is minimized to fix the remaining isogonal soft modes. Importantly, in this limiting case, the value of ϵ is immaterial as long as it is small enough (*SI Appendix*, section 2). Fig. 1*G* and Movie S1 illustrate the minimization of the cell shape energy under the angle constraints imposed by junctional force balance for the minimal setting of a perfectly symmetric cell array. The geometry is characterized by two interface lengths, ℓ_0, ℓ_1, and single angle ϕ. Incompressibility fixes ℓ_1 as a function of ℓ_0 and ϕ. We can then plot the cell shape energy $E_{\mathcal{C}}$ in a two-dimensional ϕ, ℓ_0 energy landscape. Force balance of the tensions T_0, T_1 constrains the angle $\phi = 2\arccos(T_0/2T_1)$ and relaxation of $E_{\mathcal{C}}$ takes place in the isogonal subspace parameterized by ℓ_0 (vertical white line in Fig. 1*G*), thus fully determining the cell geometry (purple dot). Changing the tensions T_0, T_1 shifts the angle constraint and therefore forces the cell shape energy to relax to a new cell geometry. By changing constraints, dynamics of the tension configuration drives tissue flow. When the tensions reach the critical ratio $T_0/T_1 = \sqrt{2}$ such that $\phi = \pi/2$, the length of the vertical interface, ℓ_0, vanishes, causing a T1 transition as discussed in the companion paper (17).

Positive Feedback and Adiabatic Dynamics. On the timescale of morphogenetic flow, tensions change due to the recruitment and release of molecular motors, driving the remodeling of the force balance geometry encoded in the tension triangulation. To complete the model, we need to specify the dynamics that governs the tensions on this slow timescale.

Based on previous experiments (27) and models (10, 28), we propose a positive feedback mechanism where tension leads to further recruitment of myosin motors and thus further increase in tension. This self-amplifying recruitment is limited by the competition for a limited pool of myosin within each cell. To mimic this effect in a computationally simple way, we constrain tension dynamics to conserve the perimeter of each tension triangle, i.e. the sum of tensions at each vertex (ijk) (see *SI Appendix*, section 2 for different local conservation laws). For an individual triangle with tensions $\tilde{T}_1$, $\tilde{T}_2$, $\tilde{T}_3$, we consider the dynamics

$$\tau_{\mathrm{T}} \partial_t \tilde{T}_\alpha = \tilde{T}_\alpha^n - \frac{1}{3}\sum_{\beta=1}^{3} \tilde{T}_\beta^n, \quad \text{with} \quad \alpha = \{1, 2, 3\}, \quad [5]$$

where n is an exponent that determines the nonlinearity of the feedback. Note that each cell–cell interface is composed of two actomyosin cortices on its two sides, and only one of the two is part of each local pool (see *SI Appendix*, section 5 for details). This feedback mechanism has a "winner-takes-all" character, where the longest edge in the tension triangle always outgrows the other two. In our model framework, we can consider a variety of possible local tension dynamics. Below we will also investigate a form of positive tension feedback that saturates, and identify the qualitative features of local tension dynamics key to the tissue dynamics.

Force balance requires that all tension triangles fit together to form a flat triangulation (13). The triangulation is parameterized by a set of 2D tension vertex positions $\mathbf{t}_i$, so that the tension on edge (ij) is given by $T_{ij} = ||\mathbf{t}_i - \mathbf{t}_j||$. In each iteration of the simulation, the tension vertices $\mathbf{t}_i$ are determined by fitting the balanced tensions T_{ij} to the intrinsic tensions $\tilde{T}_{ij}$ using a least squares method. In addition, the intrinsic tensions $\tilde{T}_{ij}$ relax to the balanced tensions T_{ij} with a rate $\tau_{\mathrm{balance}}^{-1} \ll \tau_{\mathrm{T}}^{-1}$ (see *SI Appendix*, section 5 for details. All quantifications presented here refer to the flat tensions T_{ij}.). This "balancing" of the tension triangulation effectively accounts for small pressure differentials and additional feedback mechanisms [such as the strain rate feedback (13, 14)] which maintain the tension network in a state of force balance. In particular, this ensures that cortical tensions do not lead to build-up of pressure differentials.

The above dynamics is autonomous in tension space until an edge in the cell tessellation reaches length zero. At this point, a cell neighbor exchange (T1 transition) occurs, corresponding to an edge flip in the tension triangulation. After this topological modification, the tension dynamics continues autonomously again until the next T1 event. To determine the active tension (i.e. myosin level) on the new interface formed during the cell neighbor exchange, we assume continuity of myosin concentration at vertices as described in the companion paper (17) and in *SI Appendix*, section 5. The active tension is not sufficient to balance the total tension on the new interface, such that passive elements of the cortex (e.g., cross-linkers) are transiently loaded. The resulting passive tension relaxes due to remodeling with timescale τ_{p} (*SI Appendix*, section 5) (29). This relaxation causes the elongation of the new interface, transiently counteracting positive tension feedback, and thereby prevents the new interface from immediately recollapsing after a T1.

*A degree-of-freedom count shows there is one isogonal degree of freedom per cell (13). Therefore, the isogonal modes can be parameterized by an "isogonal function" that takes a scalar value in each cell. The isogonal displacement of a vertex is defined in terms of the values of this isogonal function in the three adjacent cells (*SI Appendix, Eq.* **S8**). Note that isogonal modes are only soft if they don't deform the tissue boundary.

†As explained in *SI Appendix*, this analysis only applies for deformations in the bulk of the cell array that leaving the boundary shape unchanged.

Downloaded from https://www.pnas.org by UC Santa Barbara on July 22, 2025 from IP address 169.231.119.112.

This concludes the description of the computational model. A brief overview over the parameters and their effects is given in *SI Appendix*, Table S1 and Figs. S9 and S15 provides a flow chart of the simulation algorithm.

Results

Cell Packing Order Facilitates Self-Organized Convergent-Extension Flow. In the companion paper (17), we have shown that positive tension feedback can drive active T1 transitions in a regular lattice of cells with an initial anisotropy of tension. Any real tissue will exhibit some degree of irregularity. Therefore, investigating the effect of this disorder is key to understand CE on the tissue scale. To this end, we perform simulations of freely suspended irregular cell arrays. All parameters are set to the same values as in the companion paper, where they were calibrated to fit the tension and interface length dynamics of active T1s during *Drosophila* gastrulation (*SI Appendix*, Fig. S6).

We generated initial tension triangulations from random hard disk packings at different packing fractions ρ (30). At low packing fraction, the hard disk process generates highly irregular triangulations (Fig. 2*B*) while at sufficiently high packing fraction $\rho \gtrsim 0.72$, the disks adopt a crystalline packing such that the fraction of cells with six neighbors $p_6 \approx 1$ (Fig. 2*A*). To introduce a specified initial tension anisotropy, the triangulation is sheared with magnitude s (displacing vertices by $\mathbf{t}_i \mapsto \mathrm{diag}(\sqrt{1-s}, 1/\sqrt{1+s})\,\mathbf{t}_i$).

To quantify tension anisotropy, we define the tensor $Q = \frac{2}{3}\sum_{\alpha=1}^{3} \mathbf{T}_\alpha \otimes \mathbf{T}_\alpha$ for each triangle directly from the tension geometry. Averaging its deviatoric part $\tilde{Q} = Q - \frac{1}{2}\mathrm{Tr}\,Q$ over the cell array, provides a measure of global tension anisotropy $||\langle\sqrt{2}\tilde{Q}\rangle|| \in [0, 1]$. Starting with a slightly perturbed hexagonal cell packing and a small initial tension anisotropy, the tissue patch undergoes CE, elongating perpendicular to the initial orientation of global tension anisotropy (Fig. 2*A*).

The tissue flow is driven by self-organized cell rearrangements (active T1 transitions) whose rate rapidly increases, reaching a maximum, and then decreases to a lower, but nonzero, value (Fig. 2*F*). Large-scale tissue deformation stalls after approximately twofold CE (as measured by the square root of the aspect ratio a = width/height, Fig. 2*C*) while cells continue rearranging. T1s at this stage are no longer coherently oriented and therefore do not contribute to net tissue deformation (Fig. 2*F*).

As cells rearrange, the tissue becomes increasingly disordered, as indicated by the loss of global tension anisotropy and the decreasing fraction of cells with six neighbors, p_6 (Fig. 2*E*). The peak of tension anisotropy in the ordered initial condition coincides with the onset of T1 transitions and the decay of p_6 (*SI Appendix*, Fig. S9).

By contrast, initializing the simulation with a low level of order in the initial cell packing, but identical tension anisotropy, results in slower convergent-extension flow and arrest of flow at a smaller amount of total tissue-scale deformation (Fig. 2 *B* and *C* and Movie S2). Notably, tension anisotropy rapidly vanishes without the transient increase observed in the simulation starting with a more ordered cell packing (Fig. 2*E*). While the early dynamics depends sensitively on the initial condition, we find rapid convergence toward a common disordered steady state.

The heatmap in Fig. 2*D* shows the dependence of CE on the initial configuration as controlled by ρ and s. The total extent of CE, quantified by the net change in aspect ratio $\sqrt{a_{\mathrm{final}}/a_{\mathrm{initial}}}$

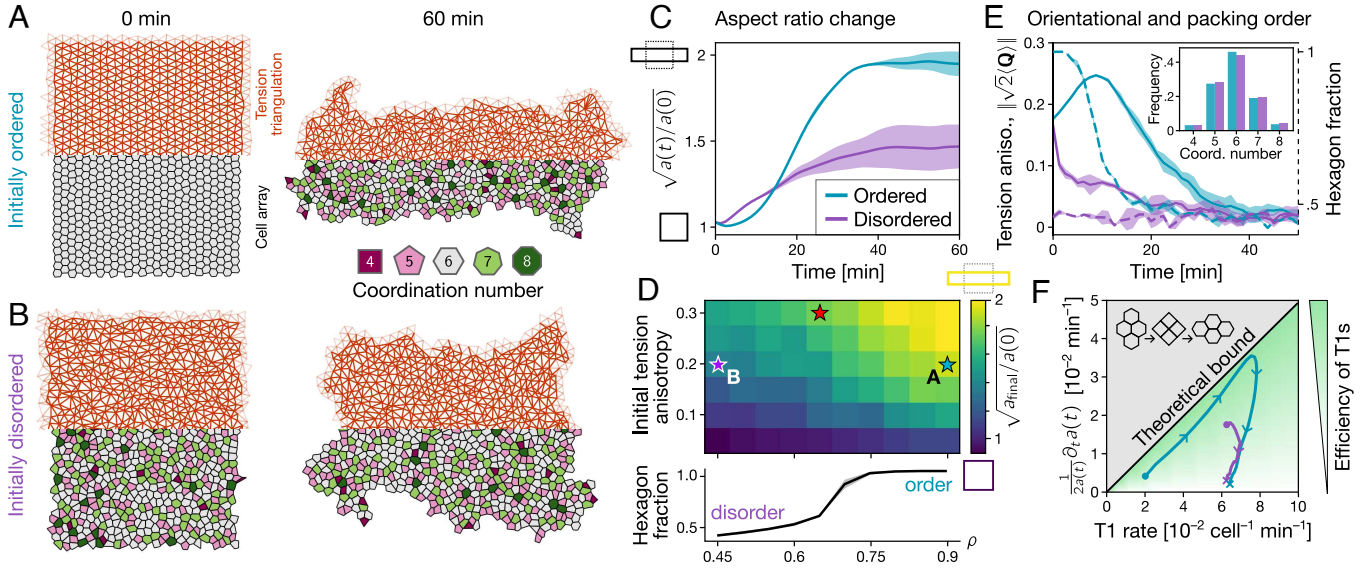

Fig. 2. Extent of tissue flow depends on initial cell-scale order and tension anisotropy. (*A* and *B*) Simulation snapshots of tissue patches with free boundaries starting from an (irregular) hexagonal cell array (*A*) and a disordered cell array (*B*) generated from a random Voronoi tessellation. A small initial tension anisotropy orients convergent-extension flow. Snapshots show the *Top* half of the tension triangulation and the *Bottom* half of the corresponding cell array. (*C*) CE [measured by the tissue aspect ratio $a(t)$] is slower and ceases at a smaller net deformation for a disordered initial condition (cyan line) compared to the initially ordered case (purple line). Shaded bands indicate SD over $N = 3$ simulation runs with $N_{\mathrm{cells}} \approx 10^3$ cells each. (*D*) The total aspect ratio change $a_{\mathrm{final}}/a(0)$ increases as a function of cell packing order (hexagon fraction controlled by hard disk packing fraction ρ used to generate the Voronoi seed points; see *Bottom* plot) and initial tension anisotropy (controlled by a shear s applied to the tension triangulation). The red star indicates the approximate state of the *Drosophila* germ band at the onset of germ band extension (cf. *SI Appendix*, Figs. S1*B* and S2), corresponding to a 1.85× elongation. (*E*) Decreasing hexagon fraction (solid lines) and global tension anisotropy (dashed lines) indicate the decay of order in the cell arrays. Notably, in the initially ordered cell array, tension anisotropy transiently increases due to positive tension feedback (solid purple line). At late times both simulations converge to zero global tension anisotropy and identical coordination number statistics (*Inset*). (*F*) Plotting the rate of tissue CE against the T1 rate provides a measure for the efficiency of T1 transitions. For the initially ordered tissue, the efficiency of T1s is starts out near the theoretical optimum ($\frac{1}{2}\log 3$ elongation for one T1 per cell as illustrated in the *Inset* cartoon) but drops to zero as the tissue becomes disordered.

Downloaded from https://www.pnas.org by UC Santa Barbara on July 22, 2025 from IP address 169.231.119.112.

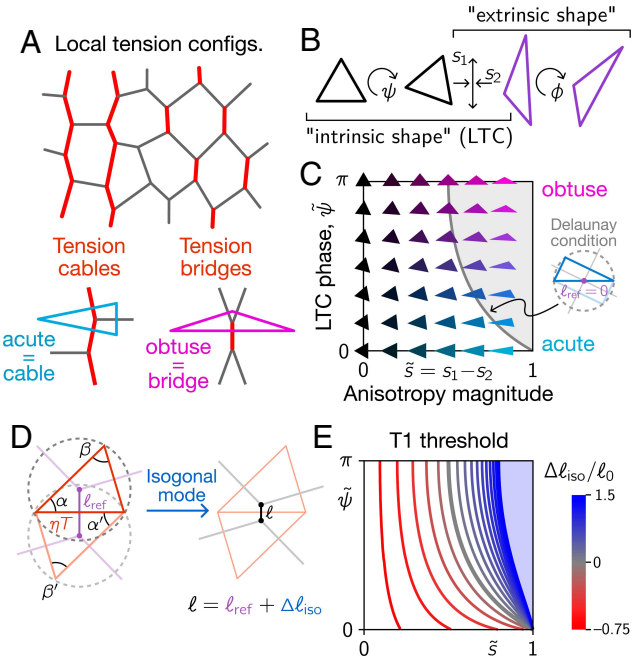

Fig. 3. Triangle shape space characterizes the local tension motifs that underlie cell rearrangements. (*A*) Local tension configurations, "cables" and "bridges," can be quantified in terms of the tension triangle shapes. (*B*) Shape decomposition of a triangle into a sequence of three transformations acting on an equilateral reference triangle. The angle ψ and the stretch factors $s_{1,2}$ determine the intrinsic shape of the triangle while the angle ϕ determines its orientation in space. (*C*) Intrinsic shape space of triangles parameterized by anisotropy (LTC magnitude) $\tilde{s}$ the "LTC phase" $\tilde{\psi}$ that distinguishes obtuse and acute triangles. The gray line indicates the Delaunay condition for a pair of identical triangles. Along this line, the circumcenters of the two triangles coincide, corresponding to a fourfold vertex in the Voronoi tessellation. (*D*) Circumcircle construction of the Voronoi edge length ℓ_{ref} (purple) from a pair of adjacent (tension) triangles (red). Circumcircles are indicated by gray dashed lines. The actual physical length ℓ is the sum of the Voronoi reference length ℓ_{ref}, and a contribution from isogonal strain $\Delta\ell_{iso}$. In the illustration, $\Delta\ell_{iso}/\ell_0$ is negative. (*E*) T1 threshold as a function of the isogonal strain $\Delta\ell_{iso}/\ell_0$. Positive isogonal strain shifts the threshold to higher tension anisotropy.

increases as a function of the initial order and the magnitude of tension anisotropy. The degradation of order through cell rearrangements means that the system dynamically traverses the phase space spanned by order p_6 and anisotropy $||\langle\sqrt{2}\tilde{Q}\rangle||$ and the remaining extension is predicted by the instantaneous value of these two quantities (*SI Appendix* Fig. S5).

We find that all simulations converge to a disordered state where T1s are incoherent and tissue flow stalls. This naturally explains key aspects of germ-band extension in the *Drosophila* embryo, in particular the transition from the fast to the slow phase of germ-band extension (17), concomitant with an increase in cell-scale disorder, approaching a maximally disordered state (17, 31) (see experimental data in *SI Appendix*, Fig. S5). The self-limiting character of CE driven by positive tension feedback is robust across variations of the tension dynamics model (*SI Appendix*, Fig. S9, section 2, and Table S1) and a similar phenomenon was observed in a recent model by Sknepnek et al. (10).

Order in Local Tension Configurations. So far, we have focused on the role of tension anisotropy and initial topological order in the cell packing. In the *Drosophila* germ band, we additionally observed a more subtle form of geometric order—a particular pattern of alternating high and low tensions (17)—that arises dynamically before the onset of cell rearrangements. The elementary motifs of a cell-scale tension pattern are the tension triangles at individual vertices. Acute triangles correspond to tension cables (adjacent high tension interfaces) while obtuse triangles—to which we refer as a tension "bridges"—are the elementary motif of an alternating pattern of high and low tensions (Fig. 3*A*).

To quantify the relative abundance of these motifs and compare our simulations to experimental data we define a local tension configuration (LTC) order parameter that measures how anisotropic and how acute vs. obtuse a given tension triangle is. To construct this order parameter, the three tension vectors $\mathbf{T}_\alpha$, $\alpha = 1, 2, 3$ that form the tension triangle are first ordered by increasing length, i.e. $T_1 \le T_2 \le T_3$, and then combined into a 2×2 matrix

$$\mathfrak{T} = \frac{1}{\sqrt{2}\mathcal{N}} \begin{pmatrix} T_1^x - T_2^x & T_1^y - T_2^y \\ \sqrt{3}\, T_3^x & \sqrt{3}\, T_3^y \end{pmatrix}. \qquad [6]$$

The normalization factor $\mathcal{N}$ ensures $||\mathfrak{T}||^2 = \mathrm{Tr}[\mathfrak{T}\mathfrak{T}^T] = 1$, fixing the arbitrary overall tension scale. $\mathfrak{T}$ is not a symmetric matrix and its indices belong to different spaces: The lower index labels the barycentric component and the upper index the Cartesian coordinate. We now carry out a singular value decomposition (SVD, geometrically illustrated in Fig. 3*B*):‡

$$\mathfrak{T} = R(\psi) \cdot \begin{pmatrix} \sqrt{s_1} & 0 \\ 0 & \sqrt{s_2} \end{pmatrix} \cdot C \cdot R^T(\phi), \qquad [7]$$

where $R(\alpha)$ is the rotation matrix with angle α, the singular values are ordered $s_1 > s_2 > 0$ by convention, and $s_1 + s_2 = 1$ because we have normalized the tension vectors. The reflection matrix $C = \mathrm{diag}(1, \pm 1)$ accounts for the chirality of the tension triangle (i.e. whether the edges go clockwise or counterclockwise if sorted by length). The angle ϕ represents the orientation of tension anisotropy in physical space. Indeed, the triangle anisotropy tensor Q defined above is given by $Q = \mathfrak{T}^T\mathfrak{T}$. The intrinsic rotation angle $\psi \in [0, \pi/6]$ controls whether the subsequent shear $\mathrm{diag}(\sqrt{s_1}, \sqrt{s_2})$ makes the triangle obtuse or acute. The intrinsic shape properties of the triangle are therefore parameterized by the magnitude of anisotropy $\tilde{s} := (s_1 - s_2) \in [0, 1]$ and the "LTC phase" $\tilde{\psi} = 6\psi \in [0, \pi]$ mapping out a two-dimensional shape space, which we refer to as LTC space (Fig. 3*C*).

The SVD Eq. **7** links two spaces with different symmetries, the hexatic symmetry of the tension triangulation with the nematic symmetry of deviatoric stress in physical space. Thus, $\mathfrak{T}$ represents a hexanematic. In to contrast the hexanematic cross-correlation defined in ref. 33, $\mathfrak{T}$ is purely local and does not depend on the magnitude of hexatic order. Moreover, the nematic order represents the orientation of deviatoric stress, not cell elongation as in refs. 33 and 34. This distinction is important because cell elongation is controlled by the isogonal modes and can therefore decouple from stress anisotropy.

A Generalized Delaunay Condition Defines the Locus of T1 Events in LTC Space. The tight coupling between tension space and physical space allows us to define a condition for the occurrence of T1 transitions in LTC space. This T1 threshold will allow us to quantify how tension dynamics causes active T1s by driving the local tension configurations toward the T1 threshold.

‡A similar decomposition was used in ref. 32 to quantify tissue strain rates from a cell-centroid-based triangulation. However, the information contained in the "LTC phase" ψ was not utilized there.

Downloaded from https://www.pnas.org by UC Santa Barbara on July 22, 2025 from IP address 169.231.119.112.

It also puts a constraint on the local tension configurations that we expect to observe.

Let us for a moment neglect the isogonal modes. From the tension triangulation we construct the corresponding Voronoi tessellation whose vertices are the circumcircle centers of the triangles as illustrated in Fig. 3*D*. The edges of the Voronoi tessellation are orthogonal to those of the triangulation, which implies that it obeys the force balance constraints, and can be used as a reference for the family of cell arrays compatible with the tension triangulation. The length of a Voronoi edge corresponding to a pair of adjacent triangles is given by

$$\ell_{\mathrm{ref}} = \frac{\sqrt{3}\,\ell_0\,T}{2}(\cot\beta + \cot\beta'), \qquad [8]$$

where T is the length of the shared triangle edge interface and ℓ_0 fixes the length scale such that $\ell_{\mathrm{ref}} = T$ for equilateral tension triangles. ℓ_{ref} changes sign at $\beta + \beta' = \pi$, which gives the "Delaunay condition" $\beta + \beta' < \pi$. In the absence of isogonal strain, a cell neighbor exchange (corresponding to an edge flip in the triangulation) must occur upon crossing this threshold. In Fig. 3*C*, the gray line indicates this threshold for a pair of identical triangles (i.e. $\beta = \beta' = \pi/2$). Notably, the threshold is at a much smaller anisotropy magnitude $\tilde{s}$ for tension cables (small $\tilde{\psi}$) than for bridges (large $\tilde{\psi}$), implying that tension cables are less efficient at driving intercalations than tension bridges.

How does the Delaunay condition generalize in the presence of isogonal strain? The length of the central interface, ℓ, can be decomposed as

$$\ell = \ell_{\mathrm{ref}} + \Delta\ell_{\mathrm{iso}}, \qquad [9]$$

where the isogonal contribution $\Delta\ell_{\mathrm{iso}}$ accounts for isogonal modes while the (Voronoi) reference length is given by Eq. **8**. Note that $\Delta\ell_{\mathrm{iso}}$ is not an edge-autonomous quantity but depends on the isogonal mode (parameterized by the isogonal function) in the four cells surrounding the interface. In practice, $\Delta\ell_{\mathrm{iso}}$ can be estimated from the average isogonal strain tensor in a local tissue patch (17). Now an interface collapses if the physical length reaches zero: $\ell_{\mathrm{ref}} + \Delta\ell_{\mathrm{iso}} = 0$. This generalizes the Delaunay condition. Fig. 3*E* shows the shifted T1 threshold as a function of the isogonal strain $\Delta\ell_{\mathrm{iso}}/\ell_0$ (see *SI Appendix* for a mathematical expression).

Winner-Takes-All Feedback Drives Coherent T1s through Formation of Tension Bridges. The LTC order parameter and the T1 threshold in hand, we can quantify the dynamics of tensions in the simulations (Fig. 4*A*) and experiments (see companion paper ref. 17 and *SI Appendix*, Fig. S2). Because isogonal strain shifts the T1 threshold (cf. Fig. 3*E*), it will have a significant effect on the LTC order parameter distribution. We imposed in our simulations the isogonal strain observed in the *Drosophila* germ band (17), where invagination of the adjacent mesoderm tissue causes isogonal strain along the axis of tension anisotropy (*SI Appendix*, section 2).

LTC histograms show an increase in anisotropy and a transient bias toward tension bridges, before convergence to a steady state biased toward tension cables as the tissue becomes disordered (Fig. 4*A*). Time traces of the median anisotropy $\tilde{s}$ and (weighted) median LTC phase $\tilde{\psi}$ show qualitative agreement with the experimental data from the *Drosophila* germ band (17) (Fig. 4*B*). Quantitative agreement can be achieved by adding constant offsets (dashed lies in Fig. 4*B*), which may be a consequence of noise in the experimental data (see *SI Appendix*, Fig. S9 for simulations incorporating Langevin noise).

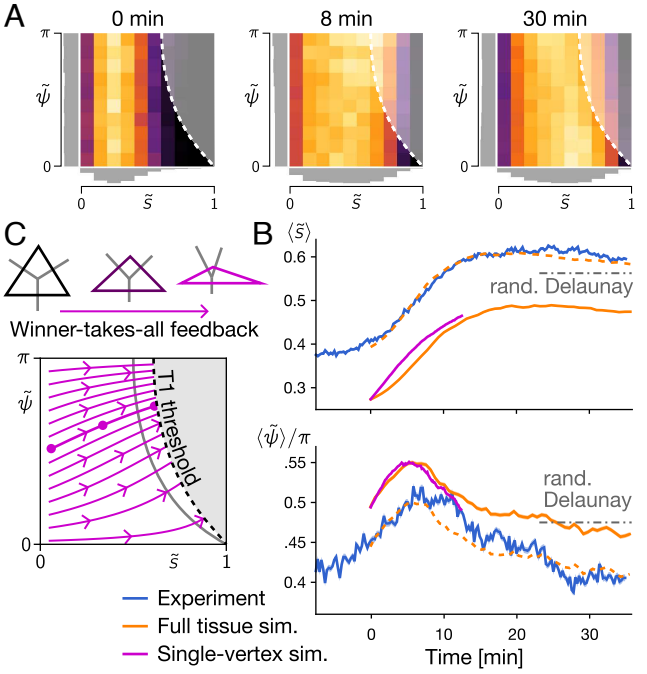

Fig. 4. Dynamics of LTC order in simulations and the *Drosophila* germ band. (*A*) Heat maps showing the distribution of local tension configurations in a simulation with imposed isogonal strain matching the experimental observations. Data aggregated from $N = 6$ simulation runs of $\sim 10^3$ cells each. (*B*) Driven by winner-takes-all feedback, the magnitude of tension anisotropy magnitude $\tilde{s}$ (*Top*) and the tension bridge fraction (measured by the LTC phase $\tilde{\psi}$; *Bottom*) increase. As the tissue becomes disordered due to cell rearrangements, the bridge fraction starts decreasing at ca. 10 min. Solid lines show the median of the LTC distributions where the phase $\tilde{\psi}$ is weighted with the magnitude $\tilde{s}$. The width of bands showing the SE is comparable to the line width. Shifting the median from simulations by a constant offset (dashed orange lines) yields a quantitative match to the experimental data. (*C*) Shape dynamics of a single tension triangle driven by winner-takes-all feedback rapidly drives the tensions toward the T1 threshold with a slight bias toward tension bridges.

To understand the LTC dynamics, consider the shape dynamics of a single, isolated tension triangle governed by winner-takes-all feedback, Eq. **5**. Starting from a configuration with nearly equal tensions, the highest tension grows at the expense of the other two, driving the triangle toward an increasingly anisotropic and obtuse shape, as illustrated in Fig. 4*C*. This LTC flow drives the tension configurations toward the T1 threshold and thereby causes the cell rearrangements. The single-triangle simulation successfully predicts early dynamics of the LTC distribution until the onset of cell rearrangements (Fig. 4*B*). The single-triangle picture also highlights the impact of isogonal strain; in simulations without imposed isogonal stretching, the T1–threshold is positioned so that bridges are rapidly eliminated by T1s (gray line in Fig. 4*C*), and no transient bride bias is observed. We predict that this will occur in twist or snail mutant embryos where mesoderm invagination is abolished.

While positive tension feedback explains the emergence of tension bridges at the local (single-triangle) level, it is not enough to produce an alternating pattern of tensions across cells. For such a pattern, tension bridges must fit together coherently, i.e. their tension anisotropy is aligned across cells. This requires that the coordination number of a majority of cells is 6, i.e. that most cells are hexagons. This explains why some degree of hexagonal packing order is required to drive coherent T1s that underlie rapid CE. Notably, however, long-range hexatic order is not necessary, as the local positive feedback on tensions is able to promote the

Downloaded from https://www.pnas.org by UC Santa Barbara on July 22, 2025 from IP address 169.231.119.112.

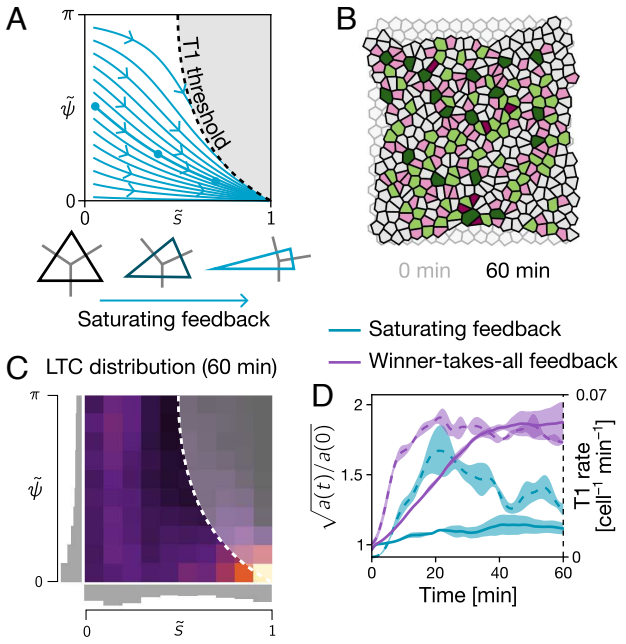

Fig. 5. Saturating tension feedback causes tension cable formation and, hence, fails to drive CE. (*A*) The flow in local tension configuration space induced by saturating positive feedback is inefficient at driving T1s. (*B*) Saturating feedback generates only little CE. The initial configuration is shown semitransparent in the background. Cell color indicates coordination number (cf. Fig. 2*A*). (*C*) The late-time LTC distribution shows a strong cable bias and differs significantly from the random Delaunay distribution emerging in simulations with winner-takes-all feedback (cf. Fig. 4*D*). (*D*) Saturating feedback (teal), compared to winner-takes-all feedback (purple), yields very little aspect ratio change and a significantly reduced T1 rate.

local alignment of hexatic and nematic order in tension space, as manifest in the LTC phase dynamics.

In Fig. 2, we have seen that as cells rearrange, the cell array becomes disordered with the coordination number statistics approaching a random Voronoi tessellation. This suggests that the corresponding tension triangulations resemble random Delaunay triangulations. To generate a family of such random triangulations, we use the same hard disk sampling method as above, controlled by the packing fraction ρ. We find that the triangle shape (LTC) statistics of a random Delaunay triangulation with $\rho \approx 0.2$ reproduces the late time statistics observed in simulations and in the *Drosophila* germ (*SI Appendix*, Fig. S3). Notably, the late-time distribution exhibits a slight bias toward tension cables. The loss of tension bridges causes active T1s to become incompatible between adjacent cells, contributing to a slowdown of tissue extension found in tissue scale simulations and in the germ band (17).

Taken together, we find that the time course of LTC distribution agrees between the model and the experimental data. Next, we show how changing aspects of the model affects the LTC distribution, highlighting that the LTC parameter can be used to distinguish different tension dynamics based on statistical signatures of cell-scale observations.

Saturating Tension Feedback Causes Tension Cable Formation and Reduced Convergent Extension. The "winner-takes-all" local tension feedback mechanism, Eq. **5**, considered so far is efficient at driving T1s because it causes the formation of tension bridges as illustrated in Fig. 4*C*. In contrast, when positive feedback rapidly saturates, adjacent high tension interfaces no longer compete, leading to the formation of tension cables (Fig. 5*A* and see *SI Appendix*, section S2 for details). The trajectories in LTC space obtained from single-triangle simulations show that saturating feedback is less efficient at driving the local tension configuration toward the T1 threshold. Indeed, tissue scale simulations with such feedback produce very little CE (see Fig. 5 *B* and *D* and Movie S3). The rate of T1 transitions is significantly reduced (Fig. 5*D*), and in contrast to "winner-takes-all" feedback, a significant fraction of T1 transitions (approximately 20%) are reversible, i.e. the newly formed edge rapidly recollapses (*SI Appendix*, section S2). Indeed, the T1 rate is transiently quite high but there is very little CE, suggesting that T1s along cables are inefficient at driving tissue deformation. Saturating tension feedback might therefore explain the reversible T1s observed in certain *Drosophila* mutants (35). As predicted from single-triangle shape-space flow (Fig. 5*A*) the LTC distribution develops a significant bias toward tension cables as shown in Fig. 5*C*. Such persistent tension cables are observed in *Drosophila abl* mutants, suggesting that knockout of *abl* might impair positive tension feedback (*Discussion*).

The above findings show that the LTC order parameters capture important structural features on the cellular scale that strongly affect the dynamics and efficiency of T1s processes. Flow in LTC parameter space obtained from single-triangle simulations serves as a simple tool to predict the cell scale behavior (efficiency of active T1s, emergence of tension cables vs. bridges) for a given tension-feedback law.

Tension-Triangulation Model Reproduces *Drosophila* Axis Elongation in a Simplified Geometry. The epithelium of the early *Drosophila* embryo forms a closed, approximately ellipsoidal surface. Therefore, deformation of one tissue region has to be compensated by an opposite deformation elsewhere. Specifically, the dorsal amnioserosa is passively stretched along the dorsoventral (DV) axis and compressed along the anterior–posterior (AP) axis to compensate the convergent extension of the germ band. To investigate this interplay of active and passive tissue deformations, we mimic the cylindrical geometry of the embryo's trunk (Fig. 6*A*) by a rectangular tissue patch with "slip walls" at the *Top* and *Bottom* boundary (Fig. 6*B*). Along the slip walls cell centroids are restricted to move along the wall, thus fixing the DV extent (i.e. "circumference") of the tissue. To account for the different mechanical properties of the lateral ectoderm and the dorsal tissue, we divide the tissue into active and passive regions (2, 17). In the former, cortical tensions are governed by positive feedback in the active region while tension homeostasis is imposed in the latter. Further, passive cells (subscript p) are taken to be soft $\mu_p = 0.2\mu_a$, $\lambda_p = 0.2\lambda_a$ compared to active cells (36). In addition, we allow interface angles in the passive region to slightly deviate from those imposed by the tension triangulation, reflecting the fact that the overall scale of cortical tensions is lower in the passive tissue (2). We initialize the simulation with a slightly perturbed hexagonal packing of cells and the experimentally observed tension anisotropy aligned along the DV axis (17).

Starting from this initial condition, the simulation reproduces salient features of the tissue-scale dynamics in the embryo (see Fig. 6*C* and Movie S4). In the active region ("lateral ectoderm," LE) active cell rearrangements drive tissue extension along the AP axis and contraction along the DV axis. The passive region ("amnioserosa," AS) is stretched along the DV axis, accommodating the fixed circumference of the embryo. Notably, this stretching leads to T1s in the passive region as is visible from the highlighted cells in Fig. 6*C*. On the tissue level, the coupling

Downloaded from https://www.pnas.org by UC Santa Barbara on July 22, 2025 from IP address 169.231.119.112.

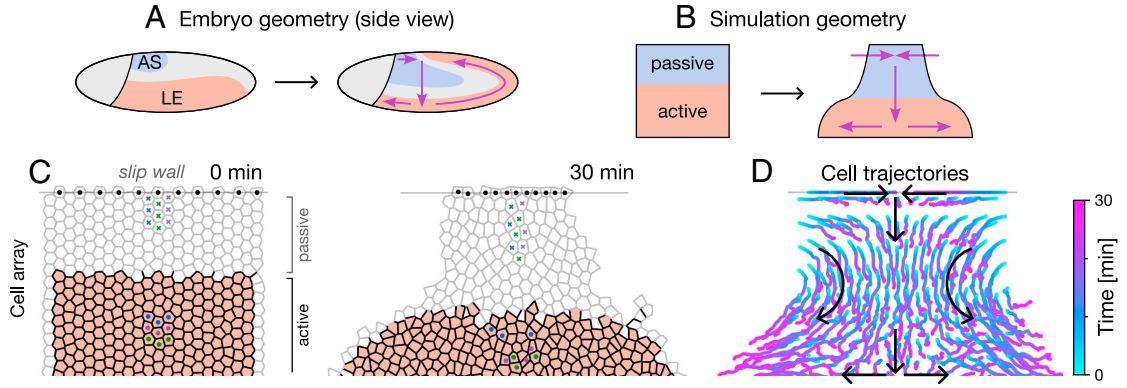

Fig. 6. Combining active and passive tissue regions. (*A* and *B*) The ellipsoidal geometry of the *Drosophila* embryo (*A*) is mimicked by a simplified simulation geometry corresponding to an unrolled cylinder (*B*), whose azimuthal axis corresponds to the dorso-ventral (vertical) axis of the embryo. The different behavior of the dorsal amnioserosa (AS) and the lateral ectoderm (LE) tissue is represented by the passive and active regions in the simulation domain respectively. (*C*) Positive feedback in the active region amplifies an initial DV anisotropy of tension and thus drives extension along the AP axis. Since the embryo's circumference is fixed (implemented via a slip wall at the dorsal boundary), the passive region is stretched along the DV axis. Only half of the simulation domain is shown, corresponding to one lateral side of the *Left–Right* symmetric embryo. Three-by-three patches of cells are highlighted to show cell rearrangements (cf. Movie S4). (*D*) Trajectories of cell centroids showing the tissue scale flow, resembling the characteristic flow of *Drosophila* germ-band extension (2).

of active and passive regions gives rise to the tissue flow pattern characteristic of *Drosophila* germ-band elongation (2) as shown in Fig. 6*D*.

Tissue Extension by Active T1s Requires Large-Scale Mechanical Patterning and Cell Shape Elasticity. The total tissue extension found in the simulations that combine active and passive tissue regions is smaller than the extension of active tissue patches with free boundaries (compare Figs. 6*D* and 2*C*). This suggests that the passive tissue resists deformation. In the following, we further investigate the role of the spatial modulation of the cells' mechanical properties along the DV axis. Fig. 7*B* shows a simulation without DV modulation where all cells are active. Positive tension feedback drives active T1s everywhere, as is manifest in the deformation of the tension triangulation (Fig. 7 *B*, *Right*). However, because of the slip-wall boundary conditions, the tissue cannot contract along the DV axis so that T1s do not result in tissue convergent extension (Movie S5; quantification in Fig. 7*C*). Instead, cell rearrangements are compensated by isogonal deformations resulting in elongated cell shapes (as quantified in Fig. 7*D*). We predict that this scenario will be realized in *Toll[RM9]* mutant embryos where all cells around the embryo's circumference adopt a ventro-lateral fate (31), as illustrated in the cartoon in Fig. 7*A*. The stretching of cells leads to a buildup of elastic energy (*SI Appendix*, Fig. S10*D*). In *Toll[RM9]* mutant embryos, some of this elastic energy is released by the formation of folds (buckling) (31) which our 2D simulations cannot capture.

Interestingly, the length dynamics of collapsing and emerging interfaces is not significantly affected by the lack of tissue-scale

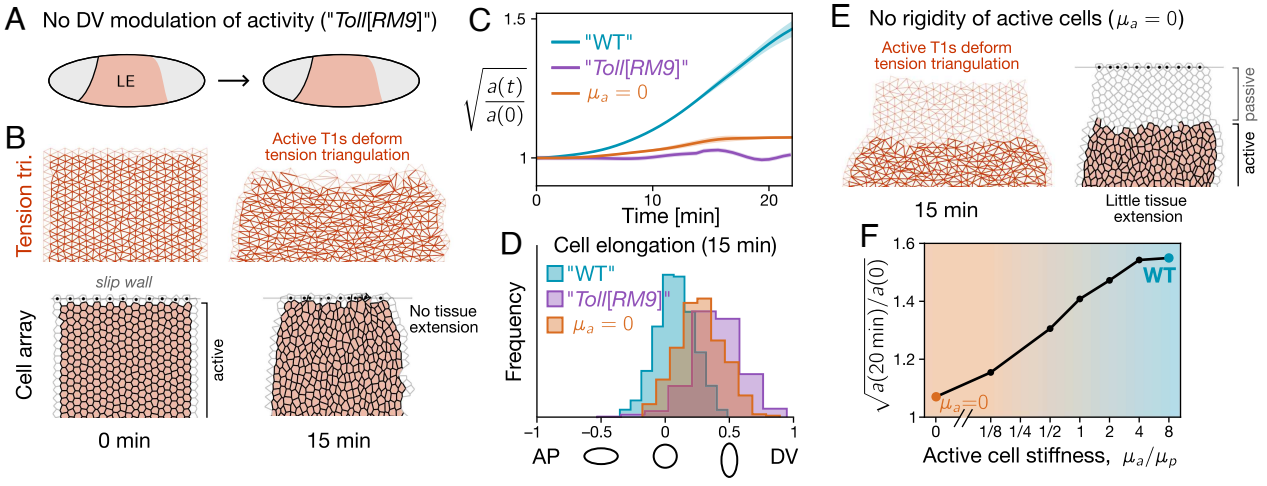

Fig. 7. Tissue flow requires cell rigidity and large-scale genetic patterning. (*A*) Cartoon of an embryo without dorso-ventral mechanical patterning, such as a *Toll[RM9]* mutant where cells all around the circumference adopt a lateral ectoderm (LE) fate. (*B*) Simulation of a tissue patch without a passive region. While active T1s deform the tension triangulation (*Top*), the cell array (*Bottom*) is blocked from elongating by the fixed DV "circumference" (implemented via slip walls). Instead, cell rearrangements are compensated by isogonal cell elongation (quantified in *D*). (*C*) CE (measured by the aspect ratio $a(t)$ of the active region) is strongly suppressed in absence of DV modulation of activity ("Toll[RM9]") and when active cells have vanishing shear modulus ($\mu_a = 0$; see *E* and *F*). (*D*) Histograms of cell shape elongation measured by relative difference, $(S_{DV,DV} - S_{AP,AP})/(S_{DV,DV} + S_{AP,AP})$, of the AP–AP and DV–DV components of the shape tensor *S*. In the WT case (cf. Fig. 6), cells remain nearly isotropic while they become significantly oriented along the DV axis when DV modulation of activity or rigidity of active cells is abolished. (*E*) When the active cells have no shear rigidity ($\mu_a = 0$), cell rearrangements are compensated by isogonal cell elongation (see *D*) without incurring an elastic energy build-up. Thus, almost no tissue-scale CE takes place. (*F*) Net amount of CE as a function of the shear modulus of active cells shows that active cells need to be stiffer than the surrounding passive tissue for active T1s to drive efficient CE.

Downloaded from https://www.pnas.org by UC Santa Barbara on July 22, 2025 from IP address 169.231.119.112.

mechanical patterning (*SI Appendix*, Fig. S10B), even though there is no tissue extension. This behavior has been observed in experiments and was interpreted as evidence for additional active mechanisms that drive interface elongation, e.g. such as medial myosin pulses (8). However, interface extension in our model is a purely passive process, resulting from the temporal asymmetry of the intercalation process (i.e. the low level of active tension on the new interface), we conclude that no such mechanisms are necessary (see *SI Appendix*, Fig. S10 for further details).

The resistance of cells against shape deformations controls the isogonal modes and therefore is an important parameter controlling the interplay of active and passive tissue deformations. Fig. 7*F* shows a simulation where the shear modulus μ_a of active cells is set to zero. Active T1s can therefore be fully compensated by cell elongation through isogonal deformations without incurring an elastic energy cost. As a result, there is no net tissue deformation (Movie S5). In other words, cell-shape rigidity is required to maintain rotund cell shapes (i.e. resist isogonal shear deformations) and thus translate active T1s into net tissue deformation. The tissue deformation by isogonal modes is determined by a balance of external forces and internal resistance of cells to the shape changes. Here, the external forces acting on the active tissue result from the passive tissue's resistance to deformation, which is in turn set by shear modulus μ_p. The ratio of the shear moduli in the active vs. the passive region, μ_a/μ_p, determines how much the active region deforms (Fig. 7*G*). Only when the cells in the active tissue are more rigid than those in the passive region ($\mu_a/\mu_p > 1$), is it energetically favorable to isogonally deform the passive region rather than the active region. This predicts that germ-band extension (GBE) can be impaired by stiffening the dorsal tissue (amnioserosa), e.g. in *dpp* mutants.

Discussion

Our model provides a theory of active elasticity based on the geometric relation (duality) between tension space and real space afforded by the force balance condition. Stabilizing feedback mechanisms that maintain adiabatic force balance are implicit in our model as we constrain the tension dynamics to the space of force-balanced configurations (flat tension triangulations). Dynamics in tension space is driven by local positive feedback. This feedback amplifies a weak initial tension anisotropy and thus drives cell shape dynamics that result in cell rearrangements (T1 processes). Notably, while active T1s are initiated by positive tension feedback, we find that their resolution is through passive relaxation of tension and does not require additional active ingredients as previously suggested (8). Force balance provides the nonlocal coupling that allows for coordination of forces and cellular behaviors across the tissue. On the tissue scale, self-organized active T1s are oriented by global tension anisotropy and thus act coherently to drive convergent-extension flow. As T1s drastically remodel tension geometry, they gradually degrade the orientational cue provided by initial tension anisotropy. (Note that this degradation of order happens locally through T1 transitions; its relation to long-wavelength instabilities of active nematics in which there are no explicit topological transitions is an interesting avenue for future research.) Thus, the locally self-organized tissue flow is generically self-limiting. It arrests after a finite extent of CE that depends on the initial degree of order in the cellular packing and the magnitude of initial tension anisotropy. This central finding suggests that cell geometry is a repository of morphogenetic information that may encode the final tissue shape.

Importantly, we show that T1s are controlled by local configuration of tensions as quantified by the LTC order parameter that links the locally hexatic space of the tension triangulation (representing force balance) with the nematic nature of deviatoric stress and strain in physical space. In contrast to previous work on "hexanematic" order in tissues (33, 34), LTC order is defined in tension space, not in physical space, and does not require (quasi-) long-range hexatic order. Moreover, the emergence of this order is not driven by a free energy but by active feedback acting on tensions as discussed further below.

Mechanically self-organized tissue dynamics provides an elegant explanation for the arrest of *Drosophila* GBE after about two-fold elongation (31), while predicting its dependence on the initial tension anisotropy (2, 14). In the companion paper (17), we used tension inference and LTC analysis to reexamine live imaging data on *Drosophila* GBE (16) showing that it is driven predominantly by the internally generated forces in the lateral ectoderm of the embryo. Quantitative analysis of imaging data confirms that *Drosophila* ectoderm starts ordered and becomes disordered as T1s proceed during CE.

Notably, while our model does not require cell-scale genetic instructions to generate local tension anisotropy(31, 37), genetic patterning on the scale of the embryo is essential for coordination and stability of global flow. In the early *Drosophila* embryo, this is manifested in the dorso-ventral patterning system that specifies the tissues with different mechanical properties and modulates mechanical feedback loops (14). We expect that the initial tension anisotropy, reported in ref. 17, is set up by anisotropic static "hoop" tension resulting from turgor pressure inside the embryo, and further reinforced by the dynamic effects of ventral furrow formation (14). An important challenge for future work is to identify the (molecular) mechanisms of both positive and negative feedback circuits, the latter stabilizing the force-balanced configuration on short timescales while the former, driving controlled remodeling on long timescales.

Our model predicts that disrupting the hexagonal packing of nuclei prior to cellularization will cause slower GBE. Interesting candidates to test this prediction are "nuclear fallout" mutants where some nuclei leave the blastoderm surface and thus introduce defects in the cellular packing (38). Another option might be the transient and partial disruption of microtubule organization with small molecule inhibitors (39). We expect that these experiments can be used to challenge and subsequently refine the model.

Comparing the LTC time courses between experiments and simulations, we find an excellent agreement, suggesting that positive feedback-driven local tension dynamics can explain cell-scale behavior during GBE. The dynamics in tension configuration space depends on the character of the positive tension feedback. Winner-takes-all feedback efficiently drives the local tension configuration toward the T1-threshold via the formation of tension bridges. By contrast, when feedback saturates at too low relative tension, it causes formation of tension cables, which had previously been suggested as a driver for CE. However, our simulations and analysis of local tension configurations show that tension cables are inefficient at driving CE, as adjacent interfaces "compete" to contract. Indeed, arrest of CE due to the formation of tension cables is also observed in recent computational studies (10, 40). When tension cables contract, they lead to formation of "rosettes" where five or more cells meet in a single vertex (41, 42). In a *Drosophila* mutant for *abl*, contraction of tension cables is impaired resulting in a reduction of rosette formation (43). By contrast, T1s appear unaffected in these mutants, suggesting that isolated high-tension junctions contract normally. Our model

Downloaded from https://www.pnas.org by UC Santa Barbara on July 22, 2025 from IP address 169.231.119.112.

offers a possible explanation of this puzzling finding: Deletion of abl might cause the positive tension feedback to saturate earlier thus leading to the formation of persistent tension cables. Taken together, the findings discussed above show that tension bridges are key to drive efficient convergent-extension flow. The LTC order parameter introduced here facilitates statistical analysis across many cells and allows one to distinguish different regimes of local tension dynamics.

Because force balance geometry does not uniquely define the shape of cells—on account of isogonal degrees of freedom—the latter play an important role in defining tissue dynamics. Isogonal soft modes account for tissue deformation under constant cortical tensions and are controlled by noncortical mechanical stresses, arising e.g. from passive cell elasticity due to cell-internal structures [e.g. nucleus (23, 24), microtubules, and intermediate filaments (25)]. We find that internal rigidity is essential to transduce cell intercalations into tissue-scale deformation against resistance from adjacent tissues. In the absence of cell resistance against deformation, intercalations are compensated by cell shape changes. However, if cell-internal elasticity becomes stronger than cortical tensions, it can resist changes in vertex angles and impede T1s and tissue flow (*SI Appendix*, Fig. S11). Such a scenario may occur in certain genetic mutants, like the "kugelkern" (*kuk*) mutant of *Drosophila*, where the nucleus is stiffer (44).

Overall, our findings suggest that epithelial tissue flows not like a fluid (where the shear modulus vanishes) but rather as a plastically deforming solid, whose remodeling is driven internally, while resisting external forces. Epithelial tissue can thus be regarded as an active solid. More generally, tissue mechanics dominated by cortical tensions that are controlled by feedback mechanisms call for a formulation of continuum mechanics that does not rely on a constitutive stress–strain relationship.

Data, Materials, and Software Availability. Simulation Code data have been deposited in GitHub (https://github.com/nikolas-claussen/CE_simulation_public/tree/ef8f315) (45).

ACKNOWLEDGMENTS. We thank Arthur Hernandez, Matthew Lefebvre, Noah Mitchell, Sebastian Streichan, and Eric Wieschaus for stimulating discussions. We further thank Dinah Loerke and Jennifer Zallen for insightful feedback. F.B. acknowledges support of the Gordon and Betty Moore Foundation postdoctoral fellowship (under grant #2919). N.H.C. was supported by National Institute of General Medical Sciences R35-GM138203 and NSF PHY. B.I.S. acknowledges support via NSF PHY: 2210612.

Author affiliations: [a]Department of Physics, University of California Santa Barbara, Santa Barbara, CA 93106; and [b]Kavli Institute for Theoretical Physics, University of California Santa Barbara, Santa Barbara, CA 93106

1. G. F. Oster, J. D. Murray, A. K. Harris, Mechanical aspects of mesenchymal morphogenesis. *Development* **78**, 83–125 (1983).
2. S. J. Streichan, M. F. Lefebvre, N. Noll, E. F. Wieschaus, B. I. Shraiman, Global morphogenetic flow is accurately predicted by the spatial distribution of myosin motors. *eLife* **7**, e27454 (2018).
3. M. Saadaoui, D. Rocancourt, J. Roussel, F. Corson, J. Gros, A tensile ring drives tissue flows to shape the gastrulating amniote embryo. *Science* **367**, 453–458 (2020).
4. A. Ioratim-Uba, T. B. Liverpool, S. Henkes, Mechano-chemical active feedback generates convergence extension in epithelial tissue. *Phys. Rev. Lett.* **131**, 238301 (2023).
5. W. Kong *et al.*, Experimental validation of force inference in epithelia from cell to tissue scale. *Sci. Rep.* **9**, 14647 (2019).
6. M. Weliky, G. Oster, The mechanical basis of cell rearrangement I Epithelial morphogenesis during Fundulus epiboly. *Development* **109**, 373–386 (1990).
7. R. Farhadifar, J. C. Röper, B. Aigouy, S. Eaton, F. Jülicher, The influence of cell mechanics, cell-cell interactions, and proliferation on epithelial packing. *Curr. Biol.* **17**, 2095–2104 (2007).
8. C. Collinet, M. Rauzi, P. F. Lenne, T. Lecuit, Local and tissue-scale forces drive oriented junction growth during tissue extension. *Nat. Cell Biol.* **17**, 1247–1258 (2015).
9. C. Duclut, J. Paijmans, M. M. Inamdar, C. D. Modes, F. Jülicher, Active T1 transitions in cellular networks. *Eur. Phys. J. E* **45**, 29 (2022).
10. R. Sknepnek, I. Djafer-Cherif, M. Chuai, C. Weijer, S. Henkes, Generating active T1 transitions through mechanochemical feedback. *eLife* **12**, e79862 (2023).
11. I. Bonnet *et al.*, Mechanical state, material properties and continuous description of an epithelial tissue. *J. R. Soc. Interface* **9**, 2614–2623 (2012).
12. N. Noll, S. J. Streichan, B. I. Shraiman, Variational method for image-based inference of internal stress in epithelial tissues. *Phys. Rev. X* **10**, 011072 (2020).
13. N. Noll, M. Mani, I. Heemskerk, S. J. Streichan, B. I. Shraiman, Active tension network model suggests an exotic mechanical state realized in epithelial tissues. *Nat. Phys.* **13**, 1221–1226 (2017).
14. H. J. Gustafson, N. Claussen, S. De Renzis, S. J. Streichan, Patterned mechanical feedback establishes a global myosin gradient. *Nat. Commun.* **13**, 7050 (2022).
15. J. Byrne, *Neuroscience Online: An Electronic Textbook for the Neurosciences* (University of Texas Houston, Houston, TX, 1997).
16. T. Stern, S. Y. Shvartsman, E. F. Wieschaus, Deconstructing gastrulation at single-cell resolution. *Curr. Biol.* **32**, 1861–1868.e7 (2022).
17. F. Brauns, N. H. Claussen, M. F. Lefebvre, E. F. Wieschaus, B. I. Shraiman, The geometric basis of epithelial convergent extension. *eLife* **13**, RP95521 (2024).
18. S. Münster *et al.*, Attachment of the blastoderm to the vitelline envelope affects gastrulation of insects. *Nature* **568**, 395–399 (2019).
19. D. Kunz *et al.*, Downregulation of extraembryonic tension controls body axis formation in avian embryos. *Nat. Commun.* **14**, 3266 (2023).
20. D. L. Farrell, O. Weitz, M. O. Magnasco, J. A. Zallen, SEGGA: A toolset for rapid automated analysis of epithelial cell polarity and dynamics. *Development* **144**, 1725–1734 (2017).
21. O. E. Jensen, E. Johns, S. Woolner, Force networks, torque balance and Airy stress in the planar vertex model of a confluent epithelium. *Proc. R. Soc. A Math. Phys. Eng. Sci.* **476**, 20190716 (2020).
22. J. C. Maxwell, On reciprocal figures and diagrams of forces. *Lond. Edinb. Dublin Philos. Mag. J. Sci.* **27**, 250–261 (1864).
23. S. Grosser *et al.*, Cell and nucleus shape as an indicator of tissue fluidity in carcinoma. *Phys. Rev. X* **11**, 011033 (2021).
24. S. Kim *et al.*, A nuclear jamming transition in vertebrate organogenesis. *Nat. Mater.*, 10.1038/s41563-024-01972-3 (2024).
25. M. Pensalfini, T. Golde, X. Trepat, M. Arroyo, Nonaffine mechanics of entangled networks inspired by intermediate filaments. *Phys. Rev. Lett.* **131**, 058101 (2023).
26. S. Wohlrab, S. Mueller, S. Gekle, Mechanical complexity of living cells can be mapped onto simple homogeneous equivalents. *Biomech. Model. Mechanobiol.* **23**, 1067–1076 (2024).
27. R. Fernandez-Gonzalez, S. D. M. Simoes, J. C. Röper, S. Eaton, J. A. Zallen, Myosin II dynamics are regulated by tension in intercalating cells. *Dev. Cell* **17**, 736–743 (2009).
28. G. Odell, G. Oster, P. Alberch, B. Burnside, The mechanical basis of morphogenesis. *Dev. Biol.* **85**, 446–462 (1981).
29. R. Clément, B. Dehapiot, C. Collinet, T. Lecuit, P. F. Lenne, Viscoelastic dissipation stabilizes cell shape changes during tissue morphogenesis. *Curr. Biol.* **27**, 3132–3142.e4 (2017).
30. E. P. Bernard, W. Krauth, D. B. Wilson, Event-chain Monte Carlo algorithms for hard-sphere systems. *Phys. Rev. E* **80**, 056704 (2009).
31. K. Irvine, E. Wieschaus, Cell intercalation during *Drosophila* germband extension and its regulation by pair-rule segmentation genes. *Development* **120**, 827–841 (1994).
32. M. Merkel *et al.*, Triangles bridge the scales: Quantifying cellular contributions to tissue deformation. *Phys. Rev. E* **95**, 032401 (2017).
33. J. M. Armengol-Collado, L. N. Carenza, L. Giomi, Hydrodynamics and multiscale order in confluent epithelia. *eLife* **13**, e86400 (2024).
34. J. M. Armengol-Collado, L. N. Carenza, J. Eckert, D. Krommydas, L. Giomi, Epithelia are multiscale active liquid crystals. *Nat. Phys.* **19**, 1773–1779 (2023).
35. P. L. Bardet *et al.*, PTEN controls junction lengthening and stability during cell rearrangement in epithelial tissue. *Dev. Cell* **25**, 534–546 (2013).
36. M. Rauzi *et al.*, Embryo-scale tissue mechanics during *Drosophila* gastrulation movements. *Nat. Commun.* **6**, 8677 (2015).
37. A. C. Paré *et al.*, A positional Toll receptor code directs convergent extension in *Drosophila*. *Nature* **515**, 523–527 (2014).
38. W. F. Rothwell, P. Fogarty, C. M. Field, W. Sullivan, Nuclear-fallout, a *Drosophila* protein that cycles from the cytoplasm to the centrosomes, regulates cortical microfilament organization. *Development* **125**, 1295–1303 (1998).
39. T. Kanesaki, C. M. Edwards, U. S. Schwarz, J. Grosshans, Dynamic ordering of nuclei in syncytial embryos: A quantitative analysis of the role of cytoskeletal networks. *Integr. Biol.* **3**, 1112 (2011).
40. J. Rozman, J. M. Yeomans, R. Sknepnek, Shape-tension coupling produces nematic order in an epithelium vertex model. *Phys. Rev. Lett.* **131**, 228301 (2023).
41. J. A. Zallen, R. Zallen, Cell-pattern disordering during convergent extension in *Drosophila*. *J. Phys. Condens. Matter* **16**, S5073–S5080 (2004).
42. J. T. Blankenship, S. T. Backovic, J. S. Sanny, O. Weitz, J. A. Zallen, Multicellular rosette formation links planar cell polarity to tissue morphogenesis. *Dev. Cell* **11**, 459–470 (2006).
43. M. Tamada, D. L. Farrell, J. A. Zallen, Abl regulates planar polarized junctional dynamics through β-catenin tyrosine phosphorylation. *Dev. Cell* **22**, 309–319 (2012).
44. A. Brandt *et al.*, Developmental control of nuclear size and shape by kugelkern and kurzkern. *Curr. Biol.* **16**, 543–552 (2006).
45. N. Claussen, CE Simulation. GitHub Repository. https://github.com/nikolas-claussen/CE_simulation_public/tree/ef8f315. Accessed 5 September 2024.

Downloaded from https://www.pnas.org by UC Santa Barbara on July 22, 2025 from IP address 169.231.119.112.